

# Anomalous Anisotropy in Superconducting Nanodiamond Films Induced by Crystallite Geometry

Gufei Zhang<sup>1,\*</sup>, Jozef Kačmarčík,<sup>2</sup> Zelin Wang,<sup>3</sup> Ramiz Zulkharnay<sup>4</sup>, Miroslav Marcin<sup>5,2</sup>, Xiaoxing Ke,<sup>3</sup> Serguei Chiriaev,<sup>1</sup> Vadzim Adashkevich,<sup>5</sup> Pavol Szabó,<sup>2</sup> Yejun Li<sup>6</sup>, Peter Samuely,<sup>2</sup> Victor V. Moshchalkov,<sup>7</sup> Paul W. May<sup>4,†</sup> and Horst-Günter Rubahn<sup>1</sup>

<sup>1</sup>*NanoSYD, Mads Clausen Institute and DIAS Danish Institute for Advanced Study, University of Southern Denmark, Alsion 2, DK-6400 Sonderborg, Denmark*

<sup>2</sup>*Centre of Low Temperature Physics, Institute of Experimental Physics, Slovak Academy of Sciences & Faculty of Science, P. J. Safarik University, Kosice, Slovakia*


<sup>3</sup>*Institute of Microstructure and Properties of Advanced Materials, Beijing University of Technology, 100124 Beijing, China*

<sup>4</sup>*School of Chemistry, University of Bristol, Bristol BS8 1TS, United Kingdom*

<sup>5</sup>*Centre of Industrial Electronics, Mads Clausen Institute, University of Southern Denmark, Alsion 2, DK-6400 Sonderborg, Denmark*

<sup>6</sup>*Hunan Key Laboratory of Super Microstructure and Ultrafast Process, School of Physics and Electronics, Central South University, 410083 Changsha, China*

<sup>7</sup>*Institute for Nanoscale Physics and Chemistry, KU Leuven, B-3001 Heverlee, Belgium*

 (Received 2 September 2019; revised manuscript received 23 October 2019; published 18 December 2019)

Tunable electronic properties upon doping make laboratory-grown nanodiamond films a promising and intriguing platform for not only refining conventional electronics, but also developing superconducting quantum devices. In a variety of superconducting systems, mostly in layered materials and heterointerfaces, superconductivity exhibits a two-dimensional (2D) character as evidenced by the anisotropy factor  $\varepsilon = \mu_0 H_{c2}^{\parallel} / \mu_0 H_{c2}^{\perp} \gg 1$ , where  $\mu_0 H_{c2}^{\parallel}$  and  $\mu_0 H_{c2}^{\perp}$  are the in-plane and out-of-plane upper critical fields, respectively. Here, we report on the observation of an anomalous anisotropy of superconductivity in heavily boron-doped nanodiamond films, which had been considered a purely three-dimensional (3D) material owing to the minute value of its coherence length in contrast to the film thickness. We investigate the resistive superconducting transition as a function of the angle of the applied magnetic field. The angular dependence of the resistive superconducting transition reveals  $\varepsilon < 1$  in the nanodiamond films, indicating an anomalous anisotropy of the superconductivity. Our structural analysis shows that the grain boundaries, particularly twin boundaries, divide the nanodiamond film into nanoscale fragments standing out of the plane. The counterintuitive anisotropic superconductivity is interpreted as a result of the quantum confinement of the superconducting order parameter in the presence of the columnar grain boundaries and intragrain twin boundaries. This research provides physical insight for developing nanodiamond-based miniaturized superconducting quantum devices by making use of the as-grown grain boundaries and/or twin boundaries.

DOI: [10.1103/PhysRevApplied.12.064042](https://doi.org/10.1103/PhysRevApplied.12.064042)

## I. INTRODUCTION

Superconducting thin films show great promise because they underpin the operation of a large variety of devices, e.g., superconducting tapes for the smart grid [1], terahertz devices for high-speed communications and astronomical detection [2,3], superconducting quantum interference devices (SQUIDs) for geomagnetic survey [4], etc. Apart from these well-known applications, superconducting thin

films have also drawn considerable attention for the emergence of intriguing phenomena as the dimensions are reduced, which can open routes to develop new functionalities and design better performing superconducting devices. The strong anisotropy of the superconductivity in quasi-two-dimensional (quasi-2D) cuprates and iron pnictides [5,6] and the heterointerface between transition metal oxides [7,8], has been studied extensively to gain insight into the pairing mechanism in unconventional superconductors.

Another intriguing superconducting material is heavily boron-doped diamond [9–11], which can be deposited in

\*gufei@mci.sdu.dk

†paul.may@bristol.ac.uk

the form of thin films using the well-developed technique of chemical vapor deposition (CVD) [12]. Superconducting diamond in the form of a polycrystalline film offers additional opportunities for the investigation of its superconducting properties as a function of parameters other than the boron-doping level. Suppression and recovery of the superconductivity in a heavily boron-doped diamond film were previously achieved by ion irradiation and annealing, respectively [13]. By decreasing the mean grain size, a systematic reduction of the coherence length was realized in a set of nanodiamond films [14]. When increasing the mean intergrain spacing or the applied pressure, a bosonic insulating state emerged in nanodiamond films as a result of suppressed intergrain Josephson coupling and localized intragrain superconducting order parameter [15–18].

Owing to the minute value of the coherence length ( $\xi < 15$  nm) [11], superconducting diamond films had previously been considered a purely three-dimensional (3D) material. It had been argued that diamond films could be treated as 2D systems for the case of films with mean grain size comparable with the film thickness [19], and so detailed reports have been devoted to unveiling 2D effects in nanodiamond films. For instance, a logarithmic divergence of the resistivity (a characteristic of 2D quantum corrections) has been reported for an 8-nm-thick nanodiamond film [20], and a 2D phase in 300-nm-thick nanodiamond films has been identified through the Azlamazov-Larkin and Lerner-Varlamov-Vinokur scaling analysis of the resistive superconducting transition [21].

Here, we show the anomalous anisotropy of superconducting nanodiamond films as revealed by angular-dependent measurements of the resistive superconducting transition in applied magnetic fields. In contrast to other superconducting thin films, where the reduced vertical dimension leads to an anisotropy factor  $\varepsilon > 1$  (see Ref. [22]), our nanodiamond films demonstrate a value for  $\varepsilon < 1$  and, thus, an out-of-plane coherence length larger than the in-plane value. By modeling the films as being composed of laterally layered diamond nanoscale fragments, we interpret the anomalous anisotropy as being a result of the confinement of the superconducting order parameter. The modeling is justified by our observation using transmission electron microscopy (TEM) of columnar grain boundaries and out-of-plane twin boundaries.

## II. EXPERIMENT

### A. Preparation of superconducting nanodiamond films

The superconducting nanodiamond films are deposited using a CVD process in a hot filament reactor [12]. In this process, a gas mixture consisting of 1% CH<sub>4</sub> in H<sub>2</sub> is passed over a tantalum filament that is resistively heated to a temperature of approximately 2000 °C. The gas

molecules thermally fragment resulting in a gaseous chemical “soup” of atoms, radicals, and ions that react together and diffuse around the chamber. Given the correct conditions, the carbon containing species crystallize onto a substrate surface to form crystalline diamond, rather than other forms of *sp*<sup>2</sup>-hybridized carbon such as graphite or fullerenes. In our case, the deposition is performed at a pressure of 20 Torr, a total gas flow of 200 sccm, and a substrate temperature of approximately 800 °C. The substrate chosen is a 1 cm<sup>2</sup> undoped single-crystal (100) silicon wafer with a 30-nm-thick SiO<sub>2</sub> layer. Growth of diamond onto this nondiamond substrate is achieved by encouraging nucleation via seeding with nanodiamond particles prior to CVD. The particles are 4–10 nm in size and electro-sprayed onto the substrate as a suspension in methanol [23], resulting in a near monolayer of nanodiamond. The subsequent CVD process enlarges these seeds, which coalesce into a continuous film adhering to the substrate. The film continues to grow vertically, in our case to a thickness of 400 nm, via a van der Drift process, which produces a columnar structure of crystalline grains separated by grain boundaries containing a few atomic layers of nondiamond *sp*<sup>2</sup>-hybridized carbon material. For boron doping, 250 ppm of B<sub>2</sub>H<sub>6</sub> gas is added to the gas mixture, resulting in a B concentration within the diamond of approximately 10<sup>21</sup> cm<sup>-3</sup>. The B is located in substitutional sites, turning the diamond into a *p*-type semiconductor at low doping levels and a metallic conductor at higher doping levels. The heavy B doping is sufficient to make our films metallic, as well as to impart superconducting behavior at temperatures less than 5 K (see Ref. [24]).

### B. Angular-dependent electrical transport measurements in magnetic fields

The electrical transport properties of the nanodiamond films are characterized in a Heliox <sup>3</sup>He cryostat by four-probe ac measurements with a lock-in amplifier. The cryostat, equipped with a dc magnet, allows electrical transport measurements in different applied magnetic fields. The angular dependence of the resistive superconducting transition is measured by rotating the nanodiamond films by varying angles with respect to the applied magnetic field.

### C. Structural analysis using TEM

For TEM observation, a cross section of the nanodiamond films is prepared by focused ion beam etching using a FEI Helios Nanolab 600i Dual Beam System. Bright-field TEM images, high-resolution TEM (HRTEM) images, and high-angle annular dark-field scanning transmission electron microscopy (HAADF STEM) images are acquired on a FEI Titan G<sup>2</sup> microscope fitted with an aberration corrector for probe-forming lens, operated at 300 kV.

### III. RESULTS AND DISCUSSION

To determine the mean grain size, a Zeiss Orion scanning helium ion microscope (SHIM) is used to image the surface of the nanodiamond films. Figure 1(a) shows the characteristic granular morphology of the samples. Digital processing of the SHIM image yields the statistics of the grain size as shown in Fig. 1(b). From the lognormal fit to the grain size distribution, the mean grain size at the surface is deduced to be approximately 270 nm. Note that this method provides an overestimate of the mean grain size, owing to the columnar, inverted pyramidlike growth mode of the diamond grains [14].

Figures 2(a) and 2(b) show the characteristic thermoresistivity  $\rho(T)$  measured in magnetic fields perpendicular and parallel to the nanodiamond films, respectively. When increasing the applied magnetic field,  $\mu_0 H$ , the superconducting state is suppressed, and the resistive superconducting transition is shifted towards zero temperature. Despite the great similarity between the two sets of data, the parallel magnetic field apparently shifts the resistive superconducting transition more efficiently to lower temperatures. To verify the difference between the influence of the perpendicular and parallel fields on the transition, we constructed the  $\mu_0 H$ - $T$  phase boundaries in Fig. 2(c) by setting the criteria at 98%, 75%, and 2% of the normal-state resistivity  $\rho_{10\text{ K}}$ , respectively, for the determination of the superconducting transition temperature at given magnetic fields. The  $\mu_0 H$ - $T$  phase boundaries as determined by the 98% $\rho_{10\text{ K}}$  and 2% $\rho_{10\text{ K}}$  criteria, approximate the onset and offset of the resistive superconducting transition, respectively.

Superconducting thin films generally show an anisotropy close to the superconducting transition temperature,  $T_c$ , because the third critical field  $\mu_0 H_{c3}$  (in plane) near  $T_c$  has a square-root-like behavior, whereas the out-of-plane

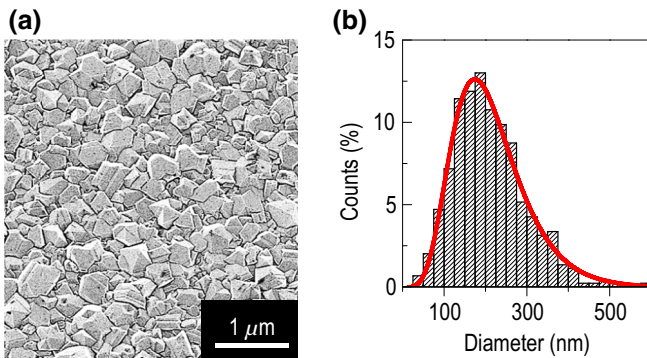


FIG. 1. Granular morphology and grain size distribution of the superconducting nanodiamond films. (a) SHIM image of the surface of the nanodiamond film. (b) Grain size statistics (displayed as a bar chart) obtained from digital processing of the SHIM image. The grain size follows a lognormal distribution (red curve).

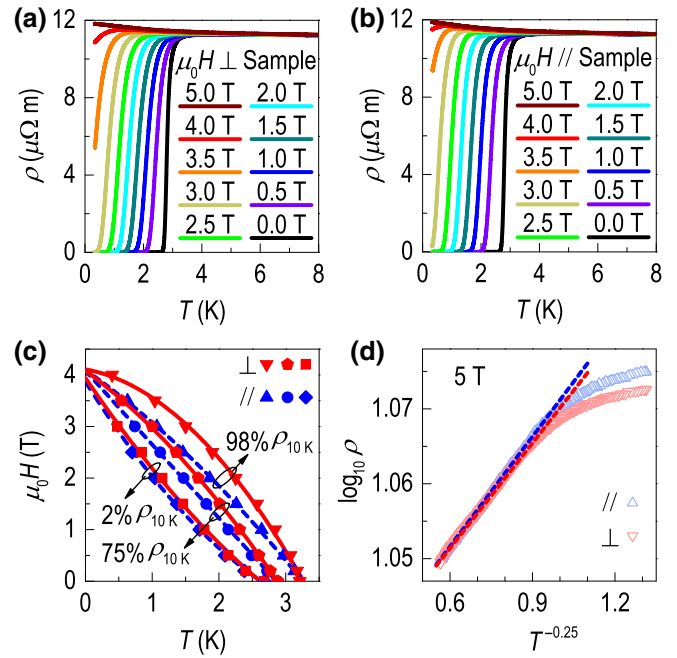


FIG. 2. Resistive superconducting transition and analysis of the fermion hopping mechanism in the nanodiamond films. (a),(b) The resistive superconducting transition is shifted towards zero temperature by magnetic fields applied perpendicular and parallel to the samples. (c) Based on the magnetic field dependence of the resistive superconducting transition, the  $\mu_0 H$ - $T$  phase boundaries are constructed by setting the criteria at 98%, 75%, and 2% of the resistivity at 10 K, respectively. The phase boundaries are extrapolated to zero temperature by quadratic fits (solid and dashed curves). (d) The thermoresistivity measured at 5 T is plotted on a semilogarithmic scale for the analysis of the fermion hopping mechanism in the insulating state. Dashed lines are fits by the variable range hopping model. The units of  $\rho$  and  $T$  are  $\mu\Omega\text{ m}$  and K, respectively.

upper critical field is always linear [25–27]. Accordingly, at first sight, the  $\mu_0 H$ - $T$  dependences as determined by the 98% $\rho_{10\text{ K}}$  criterion [see Fig. 2(c)] seem to be the  $\mu_0 H_{c3}$ - $T$  (in-plane) and  $\mu_0 H_{c2}$ - $T$  (out-of-plane) phase boundaries, respectively, as in any other superconducting thin film. In our nanodiamond films, however, the square-root-like phase boundary (inverted red triangles) is obtained in the out-of-plane fields, whereas the linearlike phase boundary (blue triangles) is measured in the in-plane fields. Thus, the square-root-like  $\mu_0 H$ - $T$  dependence (inverted red triangles) cannot be the  $\mu_0 H_{c3}$ - $T$  phase boundary as in other superconducting films but the  $\mu_0 H_{c2}^\perp$ - $T$  phase boundary of the nanodiamond films, and the linearlike  $\mu_0 H$ - $T$  dependence (blue triangles) is the  $\mu_0 H_{c2}^\parallel$ - $T$  phase boundary.

As shown in Fig. 2(c), in contrast to the negligible difference between the influence of the perpendicular and parallel fields on the offset of the resistive superconducting transition, the  $\mu_0 H$ - $T$  phase boundaries as determined by

the 98% $\rho_{10\text{ K}}$  criterion distinctly deviate from each other at temperatures below the onset critical temperature and above zero. The deviation indicates that the upper critical field in the out-of-plane direction  $\mu_0 H_{c2}^\perp$  is larger than the in-plane critical field  $\mu_0 H_{c2}^\parallel$ , revealing an anomalous anisotropy of the superconductivity in the nanodiamond films. Moreover, the higher the criterion for determining the  $\mu_0 H$ - $T$  phase boundaries, the more pronounced the anomalous anisotropy (the larger the deviation between the phase boundaries measured in perpendicular and parallel fields) at temperatures below the onset critical temperature and above zero.

When extrapolating the phase boundaries down to zero temperature, we find that all the  $\mu_0 H$ - $T$  phase boundaries as determined by the 98% $\rho_{10\text{ K}}$  and 2% $\rho_{10\text{ K}}$  criteria are in good agreement with quadratic fits [see Fig. 2(c)]. Furthermore, all the phase boundaries converge nearly at the same point at zero temperature, suggesting the possible presence of a quantum critical point. The quadratic fits yield a zero-temperature upper critical field of  $\mu_0 H_{c2}^\perp(0\text{ K}) = \mu_0 H_{c2}^\parallel(0\text{ K}) \sim 4.1\text{ T}$ , which gives rise to a Ginzburg-Landau coherence length of  $\xi_{\text{GL}} = [\Phi_0/2\pi H_{c2}(0\text{ K})]^{0.5} = 9\text{ nm}$  with  $\Phi_0 = h/2e$  being the flux quantum.

In a relatively high magnetic field of 5 T, the nanodiamond films demonstrate an insulating state. By plotting the thermoresistivity as a function of  $T^{-0.25}$  on a semilogarithmic scale, we analyze the fermion hopping mechanism, as shown in Fig. 2(d). It is found that the high-temperature part of the  $\rho(T)$  curves are in good agreement with the variable range hopping model (Mott's law in three dimensions)

$$\rho = \rho_0 \exp \left[ \left( \frac{T_0}{T} \right)^{0.25} \right], \quad (1)$$

where  $T_0$  characterizes the strength of single quasiparticle correlation [14,28]. The  $\rho(T)$  curves, however, deviate from the linear fits below 1.5 K, owing to the remnant superconductivity [14,15]. In contrast to the  $\rho(T)$  curve measured in the perpendicular field, the data measured in the parallel field deviate less from the theory at low temperatures. This phenomenon suggests that the applied magnetic field suppresses the superconductivity more efficiently in the in-plane direction, which is consistent with the difference between the in-plane and out-of-plane upper critical fields as shown in Fig. 2(c).

To gain further insight into the anisotropy of superconductivity, we measure the resistive superconducting transition by systematically tuning the angle of the applied magnetic field  $\theta$ . Figures 3(a) and 3(b) show the angular dependence of the resistive superconducting transition in  $\rho(T)$  and  $\rho(H)$ , respectively. When increasing  $\theta$  below  $90^\circ$ , the transition shifts towards higher temperatures/magnetic

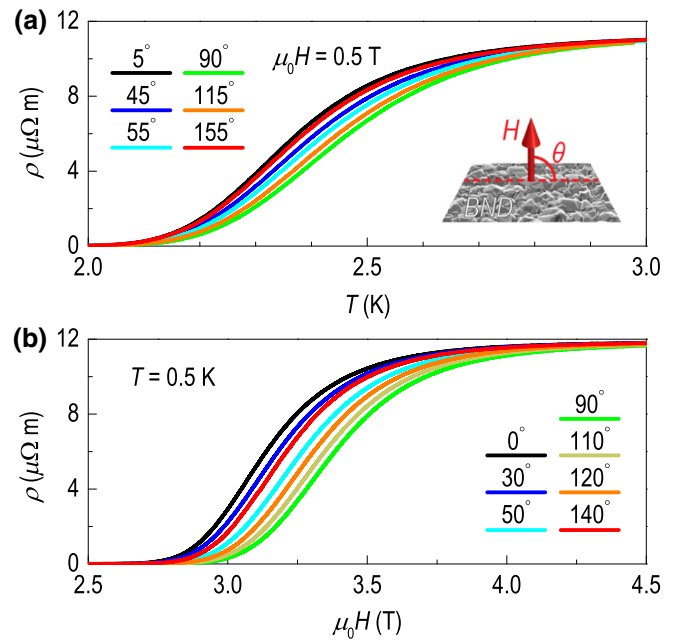


FIG. 3. Angular dependence of the resistive superconducting transition. When the applied magnetic field is oriented out of the plane, the resistive superconducting transition is shifted towards higher temperatures (a) or magnetic fields (b). Inset: Illustration of the orientation of the applied magnetic field with respect to the boron-doped nanodiamond (BND) films. Data measured at other angles are not shown for clarity.

fields. A further increase of  $\theta$  above  $90^\circ$  leads to the backward shift of the transition.

From the resistive superconducting transition in Fig. 3, we extract the angular dependences of  $T_c$  at 0.5 T [see Fig. 4(a)] and the critical field at 0.5 K [see Fig. 4(b)] by setting the criterion at 2%, 25%, 50%, 75%, and 98% of the normal-state resistivity, respectively. As shown in Fig. 4, both  $T_c$  and the critical field systematically decay when the magnetic field is oriented out of the perpendicular direction. When reaching the onset of the superconducting transition, both the decays of  $T_c$  and the critical field (the superconducting anisotropy) disappear, owing to the annihilation of the superconductivity (see Fig. 3). In the case of temperature-driven superconductor-metal transition at 0.5 T, the anomalous anisotropy is diminished close to the onset of the resistive transition [see Fig. 4(a)], whereas in the case of magnetic-field-driven phase transition at 0.5 K, the increase of the anisotropy persists even up to 98% of the transition [see Fig. 4(b)]. The difference in the temperature and field dependences of the anisotropy is because, in contrast to magnetic fields, temperature suppresses superconductivity more efficiently. The  $\mu_0 H$ - $\theta$  dependence, as determined by the 98% criterion, provides an approximation of the upper critical fields at 0.5 K, giving rise to  $\varepsilon = 0.91$ .



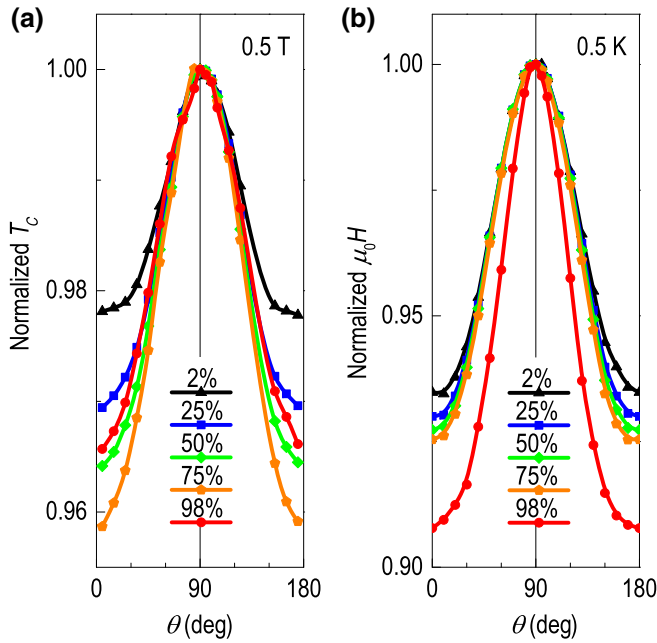


FIG. 4. Angular dependences of (a) the superconducting transition temperature in the field of 0.5 T and (b) the critical field at 0.5 K. Regardless of the criterion, all the  $T_c$ - $\theta$  and  $\mu_0 H$ - $\theta$  dependences show a systematic decay when  $\theta$  is out of  $90^\circ$ . The angular dependences of  $T_c$  and  $\mu_0 H$  are normalized to their out-of-plane values, respectively.

Based on the  $\mu_0 H$ - $\theta$  dependence in Fig. 4(b), we found that at 0.5 K  $\xi_{GL}$  ranges from 8.67 nm (in plane) to 9.53 nm (out of plane). Owing to the reduced dimension in the out-of-plane direction, superconducting thin films generally show a value for  $\varepsilon > 1$  and, thus, a larger in-plane  $\xi_{GL}$  (see Refs. [22,26]). Our nanodiamond films, however, demonstrate the opposite case, with  $\varepsilon < 1$  and a larger out-of-plane  $\xi_{GL}$ .

The Ginzburg-Landau effective mass model (GLEMM) is commonly used to analyze the anisotropy of superconducting thin films [22,29]. According to the GLEMM where only the orbital pair-breaking effect is considered [30], the angular dependence of the upper critical field  $H_{c2}(\theta)$  in a 3D system is written as

$$H_{c2}(\theta) = \frac{H_{c2}^{\parallel}}{\sqrt{\varepsilon^2 \sin^2 \theta + \cos^2 \theta}}. \quad (2)$$

Figure 5(a) shows the deviation of our experimental data from the angular dependence of the upper critical field calculated using the 3D GLEMM. When the applied magnetic field is oriented out of the perpendicular direction, the measured upper critical field decays faster than the calculated curve, suggesting an additional pair-breaking effect in our nanodiamond films, that is, the Pauli effect [31].

The anomalous superconducting anisotropy in our nanodiamond films cannot take place unless the lateral

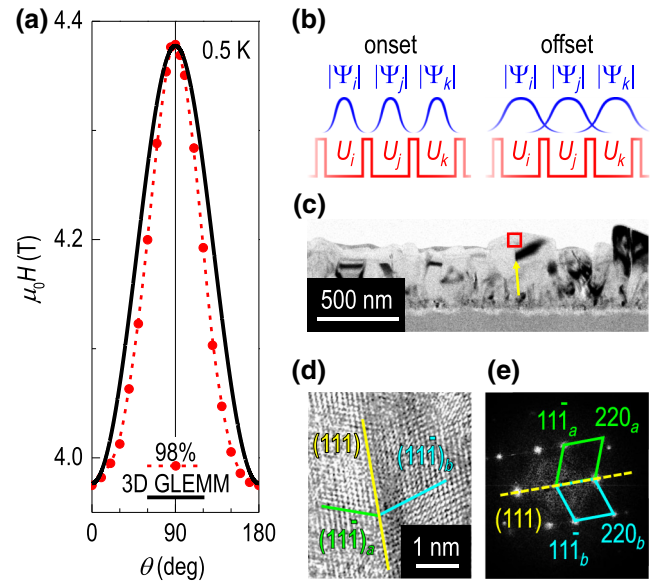


FIG. 5. Anomalous anisotropy in the superconducting nanodiamond films resulting from the confinement of the superconducting order parameter in the presence of grain and twin boundaries. (a) Angular dependences of the critical field measured at 0.5 K (red) and calculated using the 3D GLEMM (black), respectively. (b) Schematic illustration of the confinement of the superconducting order parameters  $\Psi_i$ ,  $\Psi_j$ , and  $\Psi_k$  in the potential wells  $U_i$ ,  $U_j$ , and  $U_k$ . (c) Bright-field TEM image of the cross section of the nanodiamond films. The yellow arrow indicates a characteristic twin boundary. (d) HRTEM image showing the lattice fringes and the twin boundary in the red window of (c). The yellow line is indicative of the (111) twin boundary, and the green and cyan lines indicate the (11 $\bar{1}$ ) planes at each side of the twin boundary, respectively. (e) The corresponding FFT pattern of (d). The yellow dashed line indicates the (111) mirror plane, while the rhomboids in cyan and yellow are indicative of the two sets of [1 $\bar{1}$ 0] diamond.

confinement of the superconducting order parameter,  $\Psi$ , dominates over the vertical confinement of  $\Psi$ . Accordingly, we interpret the scenario by treating the superconducting nanodiamond films as a 2D network of potential wells such as  $U_i$ ,  $U_j$ , and  $U_k$  in Fig. 5(b). Upon the onset of the resistive superconducting transition, superconducting droplets  $\Psi_i$ ,  $\Psi_j$ , and  $\Psi_k$  are formed and localized in  $U_i$ ,  $U_j$ , and  $U_k$ , respectively. Despite the macroscopic form of the thin film, the bulk behavior is mostly determined by the confinement of the superconducting order parameters in the presence of microscopic potential variations. In the case that the potential barriers generally lie approximately in the out-of-plane direction, it is easier for an in-plane field to suppress the bulk superconductivity, because the superconducting droplets are separated by nonsuperconducting barriers in this direction. Accordingly, the in-plane critical field is lower than the out-of-plane value [see Fig. 4(b)].

In the vicinity of the offset of the resistive superconducting transition, phase coherence is established over a

macroscopic scale via the proximity effect and/or Josephson coupling between the superconducting droplets. As a result of the delocalization of the superconducting order parameters, the sample becomes more like a conventional superconducting thin film rather than a 2D array of superconducting droplets from the point of view of electrical transport. Nevertheless, the anomalous anisotropy diminishes, owing to the large ratio of the film thickness to  $\xi_{GL}$ . Therefore, the  $\mu_0 H - \theta$  dependence, as determined by the 2% criterion, shows a diminished anisotropy in contrast to that of the 98% criterion [see Fig. 4(b)].

Our interpretation of the anomalous anisotropy of the superconducting nanodiamond films is justified by the observation of a large number of grain boundaries and twin boundaries in the out-of-plane direction. Figure 5(c) shows a TEM image of the cross section of the nanodiamond films. The thin film has a thickness of approximately 400 nm and is composed of diamond nanocrystallites. Grain boundaries can be clearly identified from the images, which are mostly near normal to the substrate surface, i.e., the out-of-plane direction. Twin boundaries can be further noticed from the granular thin film, and a typical twin boundary is indicated by a red arrow. HRTEM images were obtained from the twin boundary, as demonstrated in Fig. 5(d). The corresponding fast Fourier transform (FFT) pattern is shown in Fig. 5(e), and can be indexed into two sets of  $[1\bar{1}0]$  diamond, indicated by green and cyan, respectively. Therefore, a twinning plane of (111) is confirmed and indicated in both Figs. 5(d) and 5(e).

CVD diamond films often contain many twin boundaries. The mechanism for twin formation during growth is still not properly understood, but one theory is that it results from the addition to the diamond lattice of carbon species other than methyl ( $\text{CH}_3$ ), the main growth species. These other reactive species, such as  $\text{C}_2$ ,  $\text{C}_2\text{H}$ , or larger hydrocarbon radicals, are present at the growth surface in significantly lower concentrations than methyl, and so their addition to the diamond lattice is a rare event. Unlike methyl, which adds to the surface in an ordered way and propagates the diamond lattice, the other larger species have a small possibility of attaching in a way that does not follow the lattice template, i.e., crookedly, such that a second crystallite, a twin, nucleates from the first [32]. The boundaries between twins is usually atomically sharp but they can still affect the overall characteristics of the films, for example by scattering phonons thereby hindering phonon-mediated Cooper pairing and electrical transport, reducing thermal conductivity, and lowering film transparency.

Based on structural analysis, the observed anomalous anisotropy is well explained by modeling the superconducting nanodiamond films as networks of weak links (grain-boundary-grain junctions). A network composed of ordered uniform weak links should give rise to the emergence of the characteristic features of the Josephson

effect, e.g., zero-bias supercurrent, modulations of the critical current as a function of magnetic field, and oscillations of the magnetic field dependence of resistivity [33], yet no such characteristic features of the Josephson effect have been reported for granular superconducting diamond. However, Josephson-effect-like traits such as current-induced Josephson noise have been observed in nanodiamond films [34], and strong intergrain and intragrain fluctuations of the superconducting order parameter have been reported for superconducting granular diamond by scanning tunneling microscopy/spectroscopy [10,15,18]. The absence of pronounced Josephson effect in nanodiamond films is highly likely owing to the high degree of disorder. In contrast to the simplified network model, the high degree of disorder caused by the randomly oriented grain boundaries [see Fig. 1(a)], the broad grain size distribution [see Fig. 1(b)], and complex boundary conditions [10,14], can smear out the characteristic features of the Josephson effect in electrical transport measurements which characterize the bulk properties. Our interpretation suggests that the anomalous anisotropy of superconductivity will become weaker, when increasing the ratio of the lateral and vertical sizes of the nanodiamond fragments. Relevant experimental designs, however, need to fulfill the requirement that when tuning the crystallite geometry, the percolation paths for Cooper pairs should not be reduced in the granular disordered nanodiamond films.

Various miniaturized SQUIDs are being developed for advanced applications such as mesoscopic magnetic imaging [35,36] and quantum information processing [37]. As the key components of the SQUIDs, the weak links were created by either generating deformations in superconducting microstructures [38], preparing a layered system where an insulator is sandwiched in between two superconductors [35,36], or making use of the boundary between biepitaxial superconducting films [37]. The as-grown grain boundaries and twin boundaries in our superconducting nanodiamond films provide the basis for the development of diamond-based scanning nano-SQUIDs. When isolating certain grain boundaries or twin boundaries from the granular disordered diamond thin film through nanofabrication, the boundary junctions can be used as robust tips for scanning surface magnetic fields with high spatial resolution.

#### IV. CONCLUSION

By monitoring the angular dependence of the resistive superconducting transition in magnetic fields, we investigate the superconducting anisotropy of heavily boron-doped nanodiamond films. Our investigation reveals an anomalous superconducting anisotropy of this material. In contrast to 2D superconducting systems, the diamond thin films demonstrate an out-of-plane critical field higher than the in-plane value. Based on structural analysis, we

interpret the anomalous anisotropy as a result of the confinement of the superconducting order parameter in the presence of columnar grain boundaries and intragrain twin boundaries, which lie in the out-of-plane direction. Our research reveals that grain and twin boundaries can play an essential role in determining the dimensional characters of a superconducting system. Our data suggest that the naturally formed Josephson junctions at twin boundaries and grain boundaries can be used for the development of diamond-based SQUIDs.

### ACKNOWLEDGMENTS

J.K., M.M., P.Sz. and P.S. are supported by Grants No. APVV-0036-11, No. APVV-14-0605, No. VEGA 1/0409/15, No. VEGA 2/0149/16, and No. EU ERDF-ITMS 26220120005. X.K. and Z.W. acknowledge funding from the Scientific Research Project of Beijing Municipal Education Commission (Grant No. KM201610005032).

G.Z. and J.K. contributed equally to this work.

- 
- [1] T. Sudheer, M. Sarkar, A. S. Gour, V. V. Rao, and B. N. Rao, in *Proceedings From 2017 3rd International Conference on Condition Assessment Techniques in Electrical Systems*, November 16–18, Rupnagar, India (2017), p. 197.
- [2] M. Tonouchi, Cutting-edge terahertz technology, *Nat. Photonics* **1**, 97 (2007).
- [3] B. Ferguson and X.-C. Zhang, Materials for terahertz science and technology, *Nat. Mater.* **1**, 26 (2002).
- [4] T. Hato, A. Tsukamoto, S. Adachi, Y. Oshikubo, H. Watanabe, H. Ishikawa, M. Sugisaki, E. Arai, and K. Tanabe, Development of HTS-SQUID magnetometer system with high slew rate for exploration of mineral resources, *Supercond. Sci. Technol.* **26**, 115003 (2013).
- [5] T. K. Worthington, W. J. Gallagher, and T. R. Dinger, Anisotropic Nature of High-Temperature Superconductivity in Single-Crystal  $Y1Ba2Cu3O_{7-x}$ , *Phys. Rev. Lett.* **59**, 1160 (1987).
- [6] S. I. Vedenev, B. A. Piot, D. K. Maude, and A. V. Sadakov, Temperature dependence of the upper critical field of FeSe single crystals, *Phys. Rev. B* **87**, 134512 (2013).
- [7] N. Reyren, S. Thiel, A. D. Caviglia, L. Fitting Kourkoutis, G. Hammerl, C. Richter, C. W. Schneider, T. Kopp, A.-S. Rüetschi, D. Jaccard, M. Gabay, D. A. Muller, J.-M. Triscone, and J. Mannhart, Superconducting interfaces between insulating oxides, *Science* **317**, 1196 (2007).
- [8] Y. Frenkel, N. Haham, Y. Shperber, C. Bell, Y. Xie, Z. Chen, Y. Hikita, H. Y. Hwang, and B. Kalisky, Anisotropic transport at the  $LaAlO_3/SrTiO_3$  interface explained by microscopic imaging of channel-flow over  $SrTiO_3$  domains, *ACS Appl. Mater. Interfaces* **8**, 12514 (2016).
- [9] E. A. Ekimov, V. A. Sidorov, E. D. Bauer, N. N. Mel'nik, N. J. Curro, J. D. Thompson, and S. M. Stishov, Superconductivity in diamond, *Nature* **428**, 542 (2004).
- [10] G. Zhang, S. Turner, E. A. Ekimov, J. Vanacken, M. Timmermans, T. Samuely, V. A. Sidorov, S. M. Stishov, Y. Lu, B. Deloof, B. Goderis, G. Van Tendeloo, J. Van de Vondel, and V. V. Moshchalkov, Global and local superconductivity in boron-doped granular diamond, *Adv. Mater.* **26**, 2034 (2014).
- [11] E. Bustarret, J. Kačmarčík, C. Marcenat, E. Gheeraert, C. Cytermann, J. Marcus, and T. Klein, Dependence of the Superconducting Transition Temperature on the Doping Level in Single-Crystalline Diamond Films, *Phys. Rev. Lett.* **93**, 237005 (2004).
- [12] P. W. May, Diamond thin films: A 21st-century material, *Philos. Trans. R. Soc., A* **358**, 473 (2000).
- [13] D. L. Creedon, Y. Jiang, K. Ganesan, A. Stacey, T. Kageura, H. Kawarada, J. C. McCallum, B. C. Johnson, S. Praver, and D. N. Jamieson, Irradiation-Induced Modification of the Superconducting Properties of Heavily-Boron-Doped Diamond, *Phys. Rev. Appl.* **10**, 044016 (2018).
- [14] G. Zhang, S. Janssens, J. Vanacken, M. Timmermans, J. Vacík, G. W. Ataklti, W. Decelle, W. Gillijns, B. Goderis, K. Haenen, P. Wagner, and V. V. Moshchalkov, Role of grain size in superconducting boron-doped nanocrystalline diamond thin films grown by CVD, *Phys. Rev. B* **84**, 214517 (2011).
- [15] G. Zhang, T. Samuely, H. Du, Z. Xu, L. Liu, O. Onufrienko, P. W. May, J. Vanacken, P. Szabó, J. Kačmarčík, H. Yuan, P. Samuely, R. E. Dunin-Borkowski, J. Hofkens, and V. V. Moshchalkov, Bosonic confinement and coherence in disordered nanodiamond arrays, *ACS Nano* **11**, 11746 (2017).
- [16] G. Zhang, Y. Zhou, S. Korneychuk, T. Samuely, L. Liu, P. W. May, Z. Xu, O. Onufrienko, X. Zhang, J. Verbeeck, P. Samuely, V. V. Moshchalkov, Z. Yang, and H.-G. Rubahn, Superconductor-insulator transition driven by pressure-tuned intergrain coupling in nanodiamond films, *Phys. Rev. Mater.* **3**, 034801 (2019).
- [17] G. Zhang, M. Zeleznik, J. Vanacken, P. W. May, and V. V. Moshchalkov, Metal-Bosonic Insulator-Superconductor Transition in Boron-Doped Granular Diamond, *Phys. Rev. Lett.* **110**, 077001 (2013).
- [18] G. Zhang, T. Samuely, J. Kačmarčík, E. A. Ekimov, J. Li, J. Vanacken, P. Szabó, J. Huang, P. J. Pereira, D. Cerbu, and V. V. Moshchalkov, Bosonic Anomalies in Boron-Doped Polycrystalline Diamond, *Phys. Rev. Appl.* **6**, 064011 (2016).
- [19] P. Achatz, W. Gajewski, E. Bustarret, C. Marcenat, R. Piquerel, C. Chapelier, T. Dubouchet, O. A. Williams, K. Haenen, J. A. Garrido, and M. Stutzmann, Low-temperature transport in highly boron-doped nanocrystalline diamond, *Phys. Rev. B* **79**, 201203(R) (2009).
- [20] J. Bousquet, T. Klein, M. Solana, L. Saminadayar, C. Marcenat, and E. Bustarret, Phase diagram of boron-doped diamond revisited by thickness-dependent transport studies, *Phys. Rev. B* **95**, 161301(R) (2017).
- [21] C. Coleman and S. Bhattacharyya, Signature of two-dimensional transport in superconducting nanocrystalline boron-doped diamond films, *EPL* **122**, 57004 (2018).
- [22] J. Shiozaki, S. Kimura, S. Awaji, T. Nojima, and A. Tsukazaki, Anisotropy of the upper critical field and its thickness dependence in superconducting FeSe electric-double-layer transistors, *Phys. Rev. B* **97**, 174520 (2018).

- [23] O. J. L. Fox, J. O. P. Holloway, G. M. Fuge, P. W. May, and M. N. R. Ashfold, in *Diamond Electronics and Bioelectronics - Fundamentals to Applications III*, edited by P. Bergonzo, J. E. Butler, R. B. Jackman, K. P. Loh, and M. Nesládek (*Mater. Res. Soc. Symp. Proc.*, Vol. 1203, Cambridge University Press, Warrendale, PA, 2010), paper J17-27.
- [24] P. W. May, W. J. Ludlow, M. Hannaway, P. J. Heard, J. A. Smith, and K. N. Rosser, Raman and conductivity studies of boron doped microcrystalline diamond, faceted nanocrystalline diamond and cauliflower diamond films, *Diamond Relat. Mater.* **17**, 105 (2008).
- [25] E. Rosseel, M. Baert, K. Temst, C. Potter, V. V. Moshchalkov, and Y. Bruynseraede, Critical fields of W/Si multilayers, *Physica C* **225**, 262 (1994).
- [26] L. M. Joshi, A. Verma, P. K. Rout, M. Kaur, A. Gupta, and R. C. Budhani, The 2D-3D crossover and anisotropy of upper critical fields in Nb and NbN superconducting thin films, *Physica C* **542**, 12 (2017).
- [27] V. V. Moshchalkov and J. Fritzsche, *Nanostructured Superconductors* (World Scientific, New Jersey, 2011), Ch. 2.
- [28] C. Quitmann, D. Andrich, C. Jarchow, M. Fleuster, B. Beschoten, G. Güntherodt, V. V. Moshchalkov, G. Mante, and R. Manzke, Scaling behavior at the insulator-metal transition in  $\text{Bi}_2\text{Sr}_2(\text{Ca}_z\text{R}_{1-z})\text{Cu}_2\text{O}_{8+y}$  where R is a rare-earth element, *Phys. Rev. B* **46**, 11813 (1992).
- [29] S. Kittaka, T. Nakamura, Y. Aono, S. Yonezawa, K. Ishida, and Y. Maeno, Angular dependence of the upper critical field of  $\text{Sr}_2\text{RuO}_4$ , *Phys. Rev. B* **80**, 174514 (2009).
- [30] E. Helfand and N. R. Werthamer, Temperature and purity dependence of the superconducting critical field,  $H_{c2}$ . II, *Phys. Rev.* **147**, 288 (1966).
- [31] A. M. Clogston, Upper Limit for the Critical Field in Hard Superconductors, *Phys. Rev. Lett.* **9**, 266 (1962).
- [32] P. W. May, M. N. R. Ashfold, and Yu. A. Mankelevich, Microcrystalline, nanocrystalline and ultrananocrystalline diamond chemical vapor deposition: Experiment and modeling of the factors controlling growth rate, nucleation and crystal size, *J. Appl. Phys.* **101**, 053115 (2007).
- [33] P. Rödiger, P. Esquinazi, and N. García, Andreev oscillations in normal-superconducting-normal nanostructures, *J. Supercond. Nov. Magn.* **22**, 331 (2009).
- [34] J. J. Mareš, P. Hubík, J. Křištofik, and M. Nesládek, Grain boundary effects in nanocrystalline diamond, *Phys. Stat. Sol. (a)* **205**, 2163 (2008).
- [35] Z. Cui, J. R. Kirtley, Y. Wang, P. A. Kratz, A. J. Rosenberg, C. A. Watson, G. W. Gibson, Jr., M. B. Ketchen, and K. A. Moler, Scanning SQUID sampler with 40-ps time resolution, *Rev. Sci. Instrum.* **88**, 085106 (2017).
- [36] D. Vasyukov, Y. Anahory, L. Embon, D. Halbertal, J. Cuppens, L. Neeman, A. Finkler, Y. Segev, Y. Myasoedov, M. L. Rappaport, M. E. Huber, and E. Zeldov, A scanning superconducting quantum interference device with single electron spin sensitivity, *Nat. Nanotechnol.* **8**, 639 (2013).
- [37] L. Longobardi, D. Massarotti, D. Stornaiuolo, L. Galletti, G. Rotoli, F. Lombardi, and F. Tafuri, Direct Transition From Quantum Escape to a Phase Diffusion Regime in YBaCuO Biepitaxial Josephson Junctions, *Phys. Rev. Lett.* **109**, 050601 (2012).
- [38] S. Mandal, T. Bautze, O. A. Williams, C. Naud, E. Bustarret, F. Omnès, P. Rodière, T. Meunier, C. Bäuerle, and L. Saminadayar, The diamond superconducting quantum interference device, *ACS Nano* **5**, 7144 (2011).